Progress In Electromagnetics Research M, Vol. 55, 51–61, 2017

System Electromagnetic Loss Analysis and Temperature Field Estimate of a Magnetically Suspended Motor

Xiaojun Ren[1, 2, *], Yun Le[1, 2], and Bangcheng Han[1, 2]

Abstract—A magnetically suspended permanent-magnet motor (MSPMM) system mainly consists of magnetic bearings (MBs), a motor and a rotor assembly. This paper focuses on the system analysis of an MSPMM used for a vacuum turbo-molecular pump (TMP). To ensure a normal levitation and rotation, characteristics of electromagnetic field of MBs and motor are studied. For MSPMM, loss is the main heat source. To ensure the safe and steady operation of MSPMM, loss of the MB and motor are calculated and analyzed by finite element method (FEM). For thermal aspects, temperature field is estimated. Based on these analyses, the system performance can be predictive. Considering the poor heat dissipation conditions in a vacuum environment, this system analysis including loss and temperature field is of great value for MSPMM design.

1. INTRODUCTION

Brushless DC Motors (BLDCMs) have advantages of good linearity of mechanical and adjusting performance, wide adjusting speed range, long service life, convenient maintenance, low noise, and no problems caused by the brushes. So BLDCMs have great application potential in control systems [1, 2]. Magnetic bearings have numerous advantages over mechanical bearings, such as no friction, no abrasions, no lubrication, no maintenance, high speed, and high precision [3–5]. Therefore, high-speed electrical machines supported by magnetic bearings have been widely applied in industry, such as reaction wheels, control momentum gyros, energy storage flywheels, momentum wheels,high reliability compressors, and molecular vacuum pumps [6–9].

The magnetic suspension motor system mainly consists of magnetic bearings, a motor and a rotor assembly. For each separate unit, a lot of works have been done. Magnetic bearings including passive MBs [10], active MBs [11] and Hybrid MBs [12–14] are studied. Both structure design and control of electrical machines are researched by many scholars [15–21]. FEM is known as a valuable tool for solving various electromagnetic problems in electrical machines systems [22, 23]. In [24], a comprehensive definition of analytical scaling laws for PM machines was derived based on rewinding, axial scaling. Specialized motor design packages were used to verify the correctness of the derived expressions. In [25], an accurate dynamic electromagnetic model and a 2D FEM model were developed based on Tellinen hysteresis model for an asymmetric three-phase transformer. In [26], the authors presented an effective approach for calculating critical speeds of high-speed permanent magnet motor rotor-shaft assemblies. The mode analysis of the first FEM model was developed for the single shaft using software Ansys. In [27], electromagnetic characteristics combined magnetic bearing without thrust disk was analyzed by software Ansoft. However, less literature took the MBs and motor as a system to consider in MSPMM.

Received 9 January 2017, Accepted 24 February 2017, Scheduled 8 March 2017

* Corresponding author: Xiaojun Ren (renxiaojun@buaa.edu.cn).

[1] School of Instrumentation Science and Optoelectronics Engineering, Beihang University, Beijing 100191, China. [2] Beijing Engineering Research Center of High-Speed Magnetically Suspended Motor Technology and Application, Beihang University, Beijing 100191, China.

Therefore, in order to realize accurate analysis and research of MSPMM system performance, we need to consider integrated analysis. In this paper, analysis object and platform is briefly introduced firstly. Secondly, electromagnetic characteristics of MSPMM are analyzed by modeling and simulation. Thirdly, system loss of MSPMM is calculated by FEM. Fourthly, temperature fields are predicted with FEM by using the system loss as the main heat source. Finally, relative conclusion is given.

2. STRUCTURE

The object analyzed in this paper is magnetically suspended permanent-magnet electrical machines applied in a vacuum TMP. Working principle of a vacuum TMP can be simply described as momentum transfer. Rotor blades hit gas molecules, which have a high probability of being preferentially transferred to the next rotor stage after passing through the following stator stage [25].

A schematic cross section of the vacuum TMP is shown in Fig. 1(a). The vacuum TMP consists of a rotor, a motor and magnetic bearings. The spinning rotor is driven by a high-speed BLDCM and supported by two radial magnetic bearings (RMBs) and a thrust magnetic bearing (TMB). Position sensors detect the position of rotor. For startups and shutdowns, the rotor has two backup ball bearings which have a radial protective air-gap of 0.2 mm. Fig. 1(b) shows the analysis flowchart.

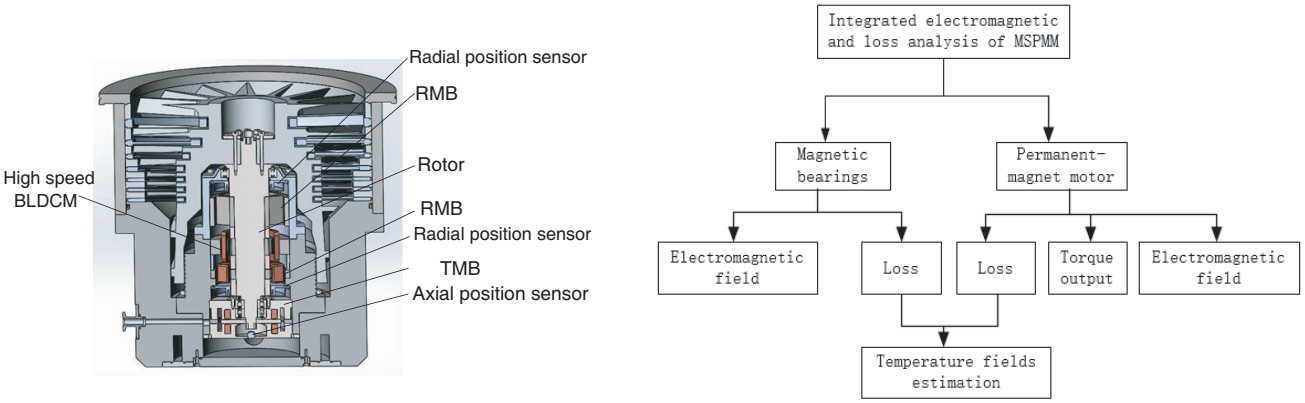

Figure 1. System structure and analysis flowchart. (a) Structure. (b) Analysis flowchart.

3. ANALYSIS OF ELECTROMAGNETIC FIELD OF MSPMM

Analysis of electromagnetic field directly affects the realization of the system function. Electromagnetic field of MB has effect on whether the rotor can be levitated normally. Electromagnetic field of motor has effect on whether the rotor rotates normally.

3.1. Electromagnetic Field of Radial MB

Due to the advantages of simple structure, easy processing and assembly, higher reliability features, radial magnetic bearing adopts a pure electromagnetic structure. The RMB system consists of two RMBs with different axial lengths. As shown in Fig. 2(a), there are eight magnetic poles on the bearing stator, which can be grouped into four magnetic pole pairs. Two adjacent poles are wired in series. Considering that the molecular pump is small, polarity sequence of NSNSNSNS is chosen for RMB. Fig. 2(b) shows the magnetic flux path. The blue solid line and red solid line denote the bias magnetic flux path and control magnetic flux path, respectively.

According to Fig. 2(b), the force expression can be obtained as

$$F_y = \frac{\mu_0 A(NI_{bias} + NI_{con})^2}{(g_0 - y)^2}\cos\alpha - \frac{\mu_0 A(NI_{bias} - NI_{con})^2}{(g_0 + y)^2}\cos\alpha \tag{1}$$

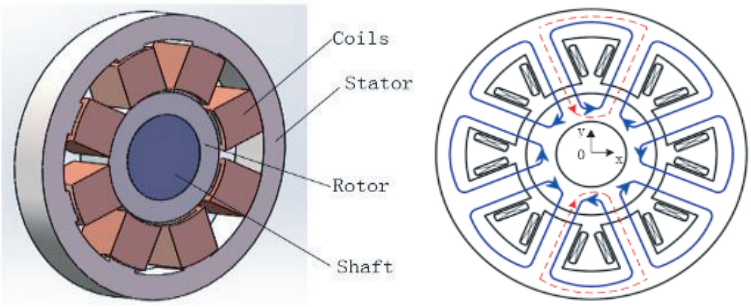

(a) (b)

Figure 2. Structure of RMB. (a) Configuration of RMB. (b) Equivalent magnetic circuit.

The current stiffness can be calculated as

$$k_{iy} = 2\mu_0 A \cos\alpha \left(\frac{NI_{bias} + NI_{con}}{(g_0 - y)^2} + \frac{NI_{bias} - NI_{con}}{(g_0 + y)^2} \right) \tag{2}$$

The current stiffness near central equilibrium position can be expressed as

$$k_{iy0} = \frac{4\mu_0 A N I_{bias} \cos\alpha}{g_0^2} \tag{3}$$

The displacement stiffness can be calculated as

$$k_{dy} = \frac{2\mu_0 A (NI_{bias} + NI_{con})^2}{(g_0 - y)^3} \cos\alpha + \frac{2\mu_0 A (NI_{bias} - NI_{con})^2}{(g_0 + y)^3} \cos\alpha \tag{4}$$

The displacement stiffness near central equilibrium position can be calculated as

$$k_{dy0} = -\frac{4\mu_0 A \cos\alpha}{g_0^3} \left(N^2 I_{bias}^2 + N^2 I_{con}^2 \right) \tag{5}$$

The maximum force can be obtained as

$$F_{\max} = \frac{4\mu_0 A N^2 I_{bias}^2 \cos\alpha}{g_0^2} \tag{6}$$

In these expressions, α is the angle between magnetic pole and y direction; here, α equals 22.5°; A is the area of one magnetic pole; μ_0 is vacuum permeability. I_{bias} and I_{con} indicate the bias and control MMF in the coil respectively. g_0 is the length of air-gap.

The bias flux density and flux path distribution are shown in Figs. 3(a) and (b), respectively. From simulation results, it can be seen that the bias magnetic density is about 0.65 T. The saturation magnetic density of iron core material is 1.4 T. Bias flux density is nearly half of saturation magnetic density. The flux density and flux path distributions with maximum current applied in $y+$ direction coils are shown in Figs. 3(c) and (d), respectively.

3.2. Electromagnetic Field of Motor

A 3D model of motor is shown in Fig. 4. Rotor, stator and windings of the motor are shown in Figs. 4(a), (b) and (c), respectively.

Assuming that the motor stator is completely symmetrical, the three-phase winding resistance and inductance coefficient are exactly the same; the three-phase winding counter electromotive force is trapezoidal wave, and the armature reaction of the stator winding is neglected. *Va*, *Vb*, *Vc* and *Vn* are the three-phase voltage and neutral point voltage, respectively; R and L are the three-phase armature winding resistance and inductance; *Ea*, *Eb* and *Ec* are the three-phase counter electromotive forces,

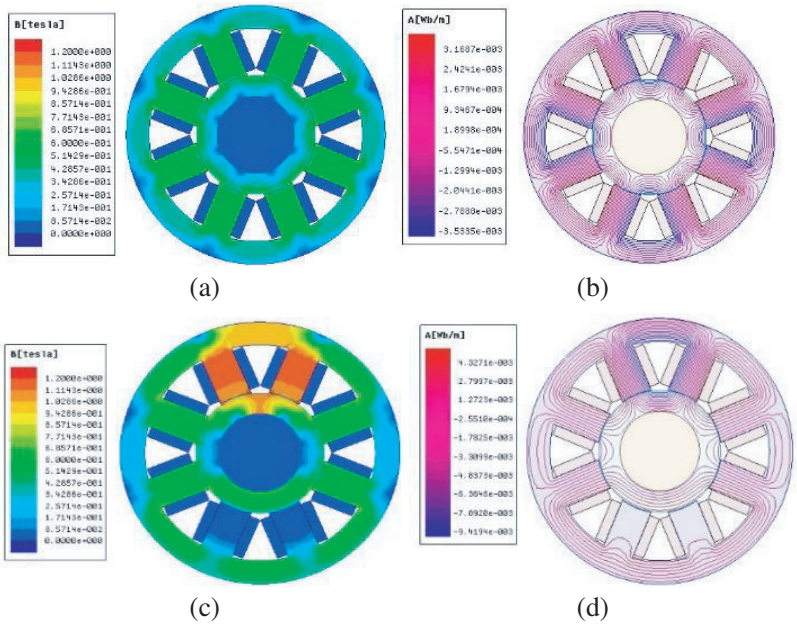

Figure 3. Magnetic field distribution of RMB. (a) Bias magnetic flux density. (b) Bias flux path. (c) Control flux density. (d) Control flux path.

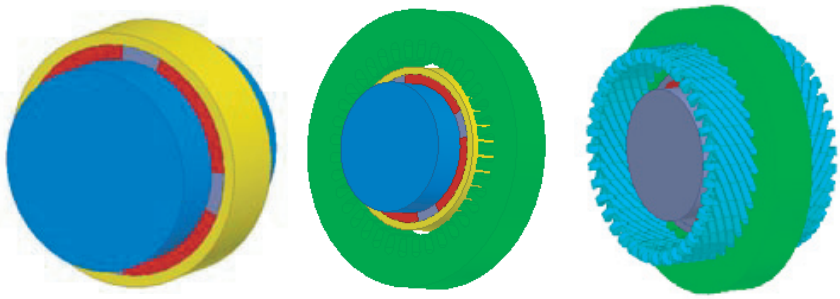

Figure 4. 3D model of motor. (a) Rotor. (b) Stator. (c) Windings.

respectively; *Ia*, *Ib* and *Ic* are the currents of three-phase winding, respectively. The mathematical model of three-phase BLDC motor is

$$\begin{cases} V_a = Ri_a + L\dfrac{di_a}{dt} + E_a + V_n \\ V_b = Ri_b + L\dfrac{di_b}{dt} + E_b + V_n \\ V_c = Ri_c + L\dfrac{di_c}{dt} + E_c + V_n \end{cases} \tag{7}$$

During the motor running, the electromagnetic torque is

$$T_e = (E_a i_a + E_b i_b + E_c i_c)/\omega \tag{8}$$

where ω is angular velocity of the rotor.

Main parameters of the motor are listed in Table 1.

Taking the symmetrical structure of the motor into account, a quarter of motor is used for simplified model in this paper. Distribution of magnetic field in electric machine, eddy loss, iron loss and torque are simulated and calculated by FEM. The magnetic field distribution scheme of the motor with no-load is shown in Fig. 5.

Table 1. Parameters of motor.

Description	Value
Rotor topology	Surface-mounted magnets
Rated speed, (r/min)	21000
Number of pole pairs	2
Inner radius of the pole shoe, (mm)	1
Rated torque, (N · m)	0.76
Width of the iron core, (mm)	24.78
Outer radius of stator, (mm)	120
Inner radius of stator, (mm)	66
Outer radius of rotor, (mm)	60
Outer radius of PM, (mm)	56
Thickness of PM, (mm)	6
Axial length of iron stator, (mm)	24
DC-link voltage, (V)	75
Phase resistance, (Ω)	0.17
Number of stator slots	36
Air gap length, (mm)	0.55
Magnet material	SmCo

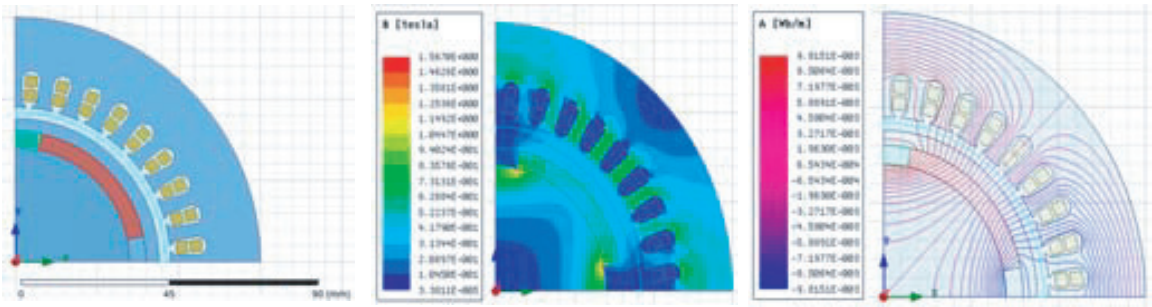

(a) (b) (c)

Figure 5. Magnetic field distribution of motor. (a) A quarter of 2D model. (b) Magnetic flux density distribution. (c) Magnetic flux path.

4. SYSTEM LOSS ANALYSIS OF MSPMM

System loss of MSPMM consists of MB loss and motor loss. When the motor is placed horizontally, the rotor rotation has little effect on the axial magnetic bearing. The iron loss of axial magnetic bearing can be ignored. Therefore, only the loss of radial MB is calculated as the loss of MB.

4.1. Loss Analysis of Radial MB

The loss curves of stator, rotor and shaft with frequency 400 Hz, 800 Hz and 1200 Hz are shown in Figs. 6(a), (b) and (c), respectively. The loss of rotor reaches 19.58 W at 1200 Hz. From Fig. 4(d), it can be seen with the increase of frequency, the stator loss increases significantly compared to that of the rotor and shaft losses. That is because the change of magnetic field of the rotor is caused by the high speed rotation. The change of magnetic field of stator is mainly caused by the change of control current.

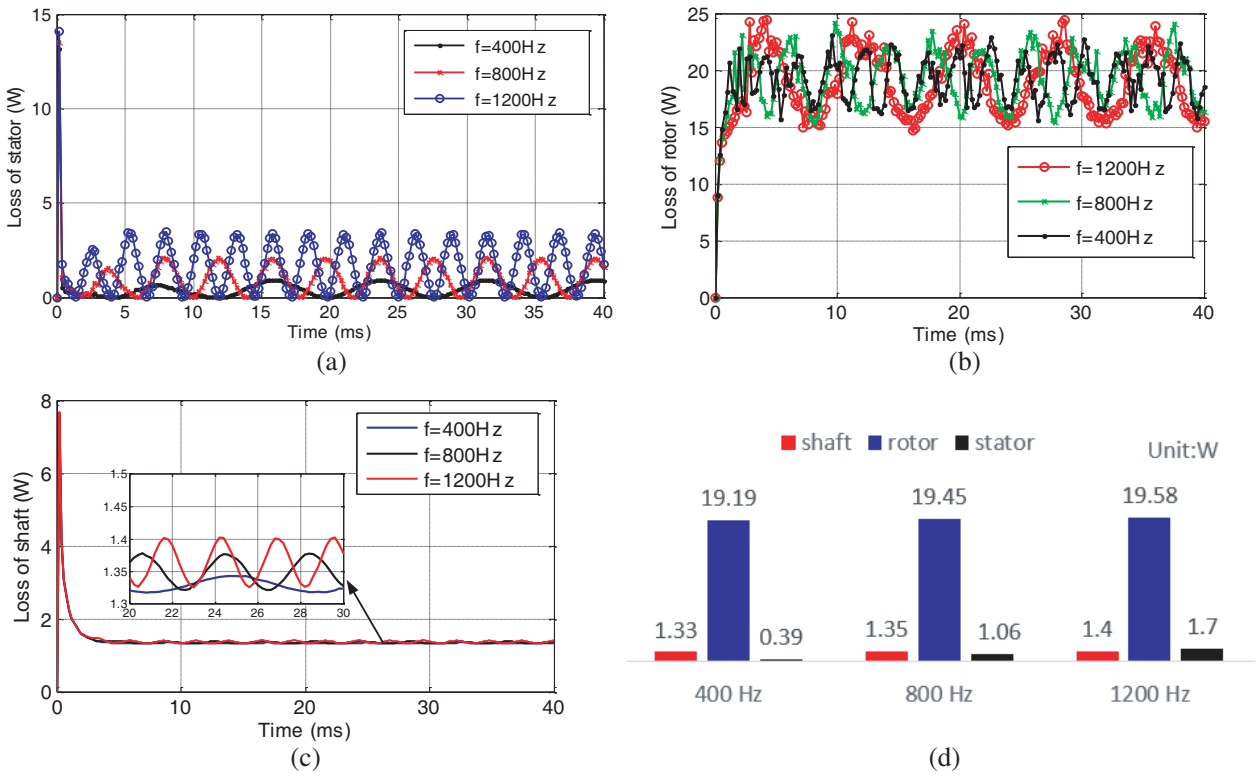

Figure 6. Loss with control current for RMB. (a) Loss curve of stator with control current. (b) Loss curve of rotor with control current. (c) Loss curve of shaft with control current. (d) Loss comparison.

4.2. Loss Analysis of Motor

Usually, the loss of a motor can be obtained by the following expression

$$P_m = P_{copper} + P_{iron} + P_{wind} \tag{9}$$

where P_{copper} denotes the copper loss; P_{iron} denotes the iron loss; P_{wind} denotes the wind loss. Since this motor is designed for a vacuum TMP, P_{wind} can be ignored.

Copper loss P_{copper} is caused by the windings. P_{copper} can be calculated as

$$P_{copper} = i^2 R \tag{10}$$

where i is the current in the winding, and R is the resistance of the windings;

The iron core loss consists of hysteresis loss and eddy-current loss [28, 29].

$$P_{iron} = \left(k_h f_r B_m^{\alpha} + k_c f_r^2 B_m^2 + k_e f_r^{1.5} B_m^{1.5}\right) V_{fe} \tag{11}$$

where k_h is the hysteresis loss coefficient; α is the Steinmetz constant; k_c is the eddy-current loss coefficient; k_e is anomalous eddy-current loss coefficient; f_r is the operating frequency; B_m is the peak flux density; V_{fe} is the volume of iron core.

Torque and loss analysis of motor are conducted by Ansoft transient simulation.

The external circuit in Simplore is shown in Fig. 7(a). The three-phase currents provided by the external circuit is shown in Fig. 7(b). The torque curve is shown in Fig. 7(c). The rated torque is 0.76 Nm. Fig. 7(d) shows eddy loss curve of the rotor when motor rotates with speed rate 21000 rpm. It is calculated that the average value of eddy loss of rotor is about 19.69 W. Fig. 7(e) shows iron loss curve of the stator when motor rotates with speed rate 21000 rpm. It is calculated that the average value of iron loss of stator is about 8.77 W. From Fig. 7, it can be seen that both the magnetic density and iron loss are in a proper range. This design not only guarantees utilization ratio of the iron core material, but also ensures a low core loss.

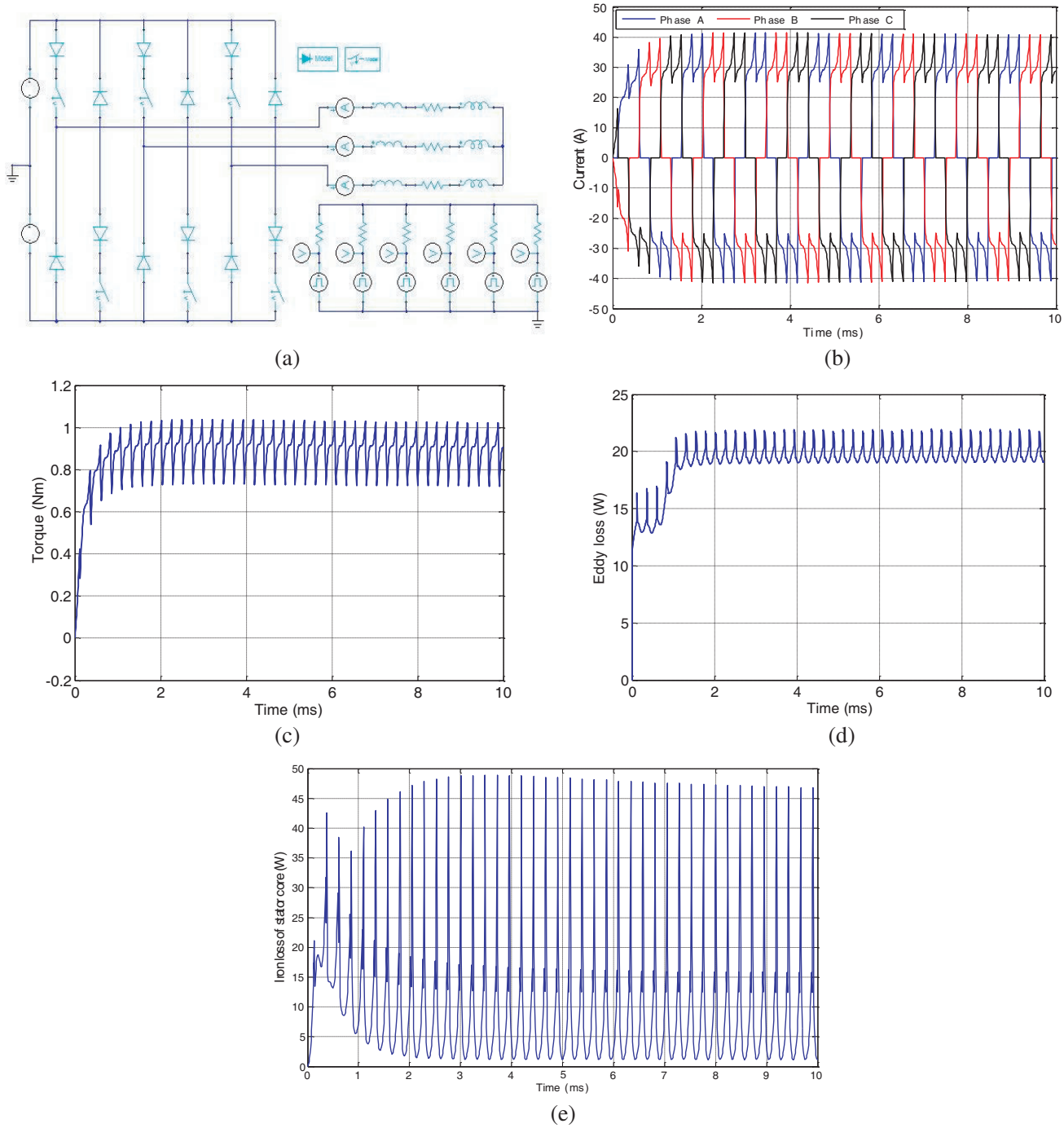

Figure 7. Torque and loss curve of motor of motor. (a) External circuit. (b) Phase currents. (c) Torque curve. (d) Eddy loss of rotor. (e) Iron loss of stator.

5. ESTIMATE OF TEMPERATURE FIELD

Thermal performance parameters of materials are listed in Table 2. The loss consumption of the whole system is analyzed. The heating components mainly consist of motor stator and rotor parts, rotor lamination and the coil part of magnetic bearing.

According to the loss values obtained in the previous simulation, heat generation rates of motor

Table 2. Parameters of materials.

Materials	Thermal conductivity ($W/(m \cdot C)$)	Radiation rate	Linear expansion coefficient ($10^{-6}/°C$)
1Cr18Ni9T′i	16.3	0.7	16.6
Sm2Co17	11	0.6	7
Silicon steel	39	0.7	19.7
40CrNiMoA	46.05	0.4	12.8
GH4169	15.3	0.5	11.8
DT4	50	0.5	12
Copper	100	0.8	9.1
7050	157	0.5	23
$2A12 - T4$	121	0.6	12

Table 3. Heat generation rate of motor assembly.

Motor assembly	stator	rotor	windings
Heat generation rate(W/m^3)	167486	4072281	3842112

Table 4. Heat generation rate of MB.

MB assembly	Stator of RMB	Rotor of RMB	Windings of RMB	Windings of TMB
Heat generation rate (W/m^3)	14100	1453430	59800	12800

assembly are listed in Table 3. Heat generation rates of RMB are calculated in Table 4. The main loss of TMB is copper loss. In steady state, rotation does not cause the variation of magnetic field. Windage loss can be neglected in vacuum environment. Therefore, loss of axial disk and stator can be neglected.

According to the heat consumption, the heat generation rate is applied in the corresponding boundary of each heating element. The heat transfer between the internal contact parts is heat conduction. Thermal conductivities are assigned to the material properties. There is heat radiation between the internal environment and the external environment. According to the individual corresponding material, heat radiation of the material is assigned to the surface of the element. Environment temperature is set at 30°C. Coefficient of heat convection for outer shell is the natural

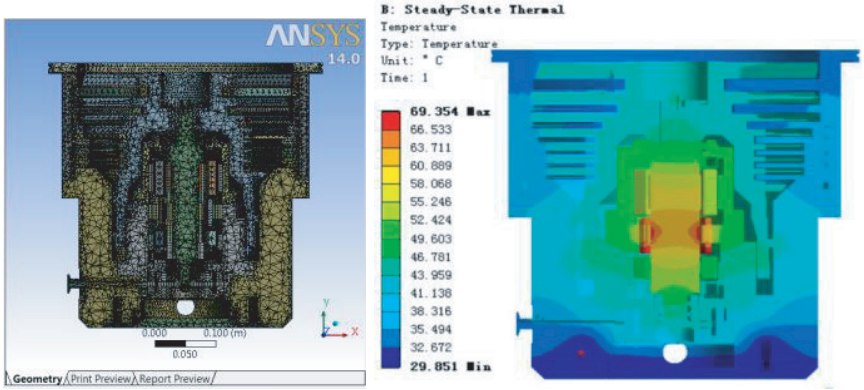

(a) (b)

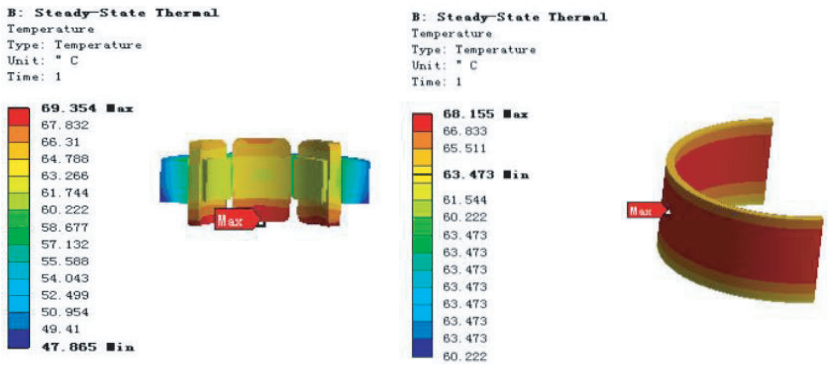

(c) (d)

Figure 8. Temperature field estimation of molecular pump. (a) FEM model. (b) Temperature field distribution. (c) Temperature field of motor stator. (d) Temperature field of motor sleeve.

convection coefficient of air, set at $9.5\,\mathrm{W}/(^{\circ}\mathrm{C}\cdot\mathrm{m}^2)$.

Thermal characteristics estimation of main components of TMP is conducted by ansys software. Fig. 8 shows temperature field distribution of TMP. The highest temperature is 69.3°C at the motor. This is because the copper loss of stator windings is relatively large. And the position gap between the motor stator and rotor is very small, so heat cannot be dissipated in time. Fig. 8(c) shows the temperature field simulation of motor stator. The highest temperature is at the stator windings. As for motor stator, the highest temperature is about 62°C. Fig. 8(c) shows the temperature field simulation of rotor sleeve. The highest temperature of sleeve is about 68.15°C.

6. CONCLUSION

This integrated analysis is very important for mechatronics products design. In this paper, integrated system analysis of magnetically suspended permanent-magnet motor is conducted. Characteristics of electromagnetic field and losses of MBs and motor are analyzed. For thermal aspects, the analysis of temperature field is also conducted based on the loss analysis. Through the analysis, it can be seen that the temperature of the permanent magnet sleeve and the winding is the highest local temperature of motor. The temperature of MB is slightly lower than the temperature of the motor. Therefore, in the design of a magnetic levitation motor used in the vacuum pump, in order to reduce the temperature, minimizing loss is necessary in the premise of ensuring the electromagnetic performance. This integrated loss analysis and system thermal predictive in design state is valuable to guarantee the implementation of system performance.

ACKNOWLEDGMENT

This work was supported by the National Natural Science Foundation of China under Grants 51605017, 61573032 and 61421063, the National Key Research and Development Program of China under Grant 2016YFB0500804, and the National Major Project for the Development and Application of Scientific Instrument Equipment of China under Grant 2012YQ040235.

REFERENCES

1. Jiang, W., H. Huang, J. Wang, et al., "Commutation analysis of brushless DC motor and reducing commutation torque ripple in the two-phase stationary frame," *IEEE Transactions on Power Electronics*, Vol. 32, No. 6, 4675–4682, 2017.
2. Kim, K.-T., S.-T. Lee, and J. Hur, "Diagnosis technique using a detection coil in BLDC motors with interturn faults," *IEEE Transactions on Magnetics*, Vol. 50, No. 2, 7021904, 2014.

3. Schweitzer, G. and E. H. Maslen, *Magnetic Bearings Theory, Design and Application to Rotating Machinery*, Springer-Verlag, Berlin, 2009.
4. Lee, T. and C. Liu, "Design and analysis of a new axial-field magnetic variable gear using pole-changing permanent magnets," *Progress In Electromagnetics Research*, Vol. 153, 23–32, 2015.
5. Ren, X. J., Y. Le, and B. C. Han, "Asymmetric electromagnetic analysis and design of a permagnet biased axial magnetic bearings," Pages: 574 - 586, DOI: 10.1109/PIERS.2016.7734394 *Progress In Electromagnetics Research Symposium*, 574–586, Aug. 2016, Shanghai, China.
6. Tang, J., J. Sun, J. Fang, et al., "Low eddy loss axial hybrid magnetic bearing with gimballing control ability for momentum flywheel," *J. Magn. Magn. Mater*, Vol. 329, 12, 2013.
7. Ren, X. J., Y. Le, J. J. Sun, et al., "Magnetic flux leakage modeling and optimization of a combined radial-axial hybrid magnetic bearing for DC motor," *IET Electric Power Applications*, to be published, DOI: 10.1049/iet-epa.2016.0259.
8. Fang, S. H., et al., "Analysis and design of a high-speed permanent magnet characteristic actuator using eddy current effect for high-voltage vacuum circuit breaker," *IET Electric Power Applications*, Vol. 10, No. 6, 268–275, 2016.
9. Han, B., S. Zheng, Y. Le, et al., "Modeling and analysis of coupling performance between passive magnetic bearing and hybrid magnetic radial bearing for magnetically suspended flywheel," *IEEE Trans. Magn.*, Vol. 49, No. 10, 5356–5370, Oct. 2013.
10. Zhang, C., K. J. Tseng, T. D. Nguyen, and G. Zhao, "Stiffness analysis and levitation force control of active magnetic bearing for a partially-self-bearing flywheel system," *International Journal of Applied Electromagnetics and Mechanics*, Vol. 36, 229–242, 2011.
11. Le, Y., J. Fang, B. Han, et al., "Dynamic circuit model of a radial magnetic bearing with permanent magnet bias and laminated cores," *International Journal of Applied Electromagnetics and Mechanics*, Vol. 46, 43–60, 2014.
12. Han, B., Q. Xu, and Q. Yuan, "Multiobjective optimization of a combined radial-axial magnetic bearing for magnetically suspended compressor," *IEEE Transactions on Industrial Electronics*, Vol. 64, No. 4, 2284–2293, 2016.
13. Fang, J., C. Wang, and T. Wen, "Design and optimization of a radial hybrid magnetic bearing with separate poles for magnetically suspended inertially stabilized platform," *IEEE Transactions on Magnetics*, Vol. 50, No. 50, 8101011, May 2014.
14. Si, M., X. Y. Yang, S. W. Zhao, and S. Gong, "Design and analysis of a novel spoke-type permanent magnet synchronous motor," *IET Electric Power Applications*, Vol. 10, No. 6, 571–580, 2016.
15. Barcaro, M., T. Pradella, and I. Furlan, "Low-torque ripple design of a ferrite-assisted synchronous reluctance motor," *IET Electric Power Applications*, Vol. 10, No. 5, 319–329, 2016.
16. Hou, Z., J. Huang, H. Liu, T. Wang, and L. Zhao, "Quantitative broken rotor bar fault detection for closed-loop controlled induction motors," *IET Electric Power Applications*, Vol. 10, No. 5, 403–410, 2016.
17. Prieto, D., P. Dessante, J.-C. Vannier, et al., "Multi-physic analytical model for a saturated permanent magnet assisted synchronous reluctance motor," *IET Electric Power Applications*, Vol. 10, No. 5, 356–367, 2016.
18. Lim, M.-S., S.-H. Chai, and J.-P. Hong, "Design and iron loss analysis of sensorless-controlled interior permanent magnet synchronous motors with concentrated winding," *IET Electric Power Applications*, Vol. 8, No. 9, 349–356, 2014.
19. Azari, M. N. and M. Mirsalim, "Analytic modelling of a line-start permanent-magnet motor with slotted solid rotor," *IET Electric Power Applications*, Vol. 8, No. 7, 278–285, 2014.
20. Huber, T., W. Peters, and J. Böcker, "A low-order thermal model for monitoring critical temperatures in permanent magnet synchronous motors," *7th IET International Conference on Power Electronics, Machines and Drives (PEMD 2014)*, 1–6, 2014.
21. Stipetic, S., D. Zarko, and M. Popescu, "Ultra-fast axial and radial scaling of synchronous permanent magnet machines," *IET Electric Power Applications*, Vol. 10, No. 7, 658–666, 2016.

22. Zhao, B., *Application of Ansoft 12 in Engineering Electromagnetic Field*, Water Power Press, Beijing, China, 2010 (in Chinese).
23. Wang, T., X. Ouyang, L. Li, and X. Li, "Optimization of the five phase fault tolerant motor based on Ansoft simulation," *IEEE/CSAA International Conference on Aircraft Utility Systems (AUS)*, 1035–1039, Beijing, China, Oct. 2016, DOI: 10.1109/AUS. 2016. 7748209.
24. Aboura, F. and O. Touhami, "Integration of the hysteresis in models of asymmetric three-phase transformer: Finite-element and dynamic electromagnetic models," *IET Electric Power Applications*, Vol. 10, No. 7, 614–622, 2016.
25. Huang, Z. Y. and B. C. Han, "Effective approach for calculating critical speeds of high-speed permanent magnet motor rotor-shaft assemblies," *IET Electric Power Applications*, Vol. 9, No. 9, 628–633, 2015.
26. Han, B., Q. Xu, and S. Zheng, "Integrated radial/thrust magnetic bearing without thrust disk for a high-speed driving system," *IET Electric Power Applications*, Vol. 10, No. 4, 276–283, 2016.
27. Huang, Z., B. Han, et al., "Mechanical stress and thermal aspects of the rotor assembly for turbo-molecular pumps," *Vacuum*, Vol. 129, 55–62, 2016.
28. Zhang, Z., L. Yu, L. Sun, L. Qian, and X. Huang, "Iron loss analysis of doubly salient brushless DC generators," *IEEE Trans. Ind. Electron.*, Vol. 62, No. 4, 2156–2163, Apr. 2015.
29. Huang, Z., J. Fang, X. Liu, and B. Han, "Loss calculation and thermal analysis of rotors supported by active magnetic bearings for high-speed permanent-magnet electrical machines," *IEEE Trans. Ind. Electron.*, Vol. 63, No. 4, 2027–2035, Apr. 2016.